ACS NANO
Cite This: ACS Nano 2019, 13, 13421−13429
www.acsnano.org
ARTICLE

Quantitative 3D Characterization of Elemental Diffusion Dynamics in Individual Ag@Au Nanoparticles with Different Shapes

Alexander Skorikov,[†,∥] Wiebke Albrecht,[†,∥] Eva Bladt,[†] Xiaobin Xie,[‡] Jessi E. S. van der Hoeven,[‡,§] Alfons van Blaaderen,[‡] Sandra Van Aert,[†] and Sara Bals*[,†]

[†]EMAT, University of Antwerp, Groenenborgerlaan 171, 2020 Antwerp, Belgium

[‡]Soft Condensed Matter, Debye Institute for Nanomaterials Science, Utrecht University, Princetonplein 5, 3584 CC Utrecht, The Netherlands

[§]Inorganic Chemistry and Catalysis, Debye Institute for Nanomaterials Science, Utrecht University, Universiteitsweg 99, 3584 CG Utrecht, The Netherlands

Supporting Information

ABSTRACT: **Anisotropic bimetallic nanoparticles are promising candidates for plasmonic and catalytic applications. Their catalytic performance and plasmonic properties are closely linked to the distribution of the two metals, which can change during applications in which the particles are exposed to heat. Due to this fact, correlating the thermal stability of complex heterogeneous nanoparticles to their microstructural properties is of high interest for the practical applications of such materials. Here, we employ quantitative electron tomography in high-angle annular dark-field scanning transmission electron microscopy (HAADF-STEM) mode to measure the 3D elemental diffusion dynamics in individual anisotropic Au−Ag nanoparticles upon heating *in situ*. This approach allows us to study the elemental redistribution in complex, asymmetric nanoparticles on a single particle level, which has been inaccessible to other techniques so far. In this work, we apply the proposed method to compare the alloying dynamics of Au−Ag nanoparticles with different shapes and compositions and find that the shape of the nanoparticle does not exhibit a significant effect on the alloying speed whereas the composition does. Finally, comparing the experimental results to diffusion simulations allows us to estimate the diffusion coefficients of the metals for individual nanoparticles.**

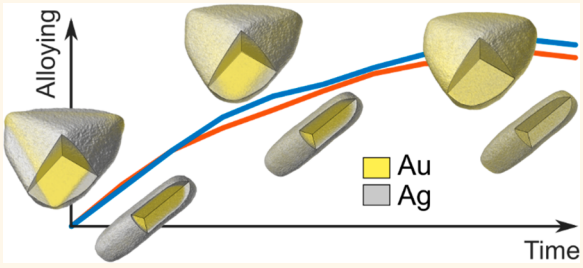

KEYWORDS: *in situ electron tomography, chemically sensitive tomography, single particle study, bimetallic nanoparticles, alloying dynamics, diffusion simulation*

Metal nanoparticles have proven to be of high value for a wide range of applications owing to their unique plasmonic, photothermal, and catalytic properties.[1−4] Next to biomedical applications such as hyperthermic cancer treatment or drug delivery,[5] metal nanoparticles are used for sensing,[6,7] data storage,[8] photovoltaics,[9] and (photo)catalysis.[10] For most applications, anisotropic shapes are beneficial due to their superior plasmonic properties compared to spherical nanoparticles, with strong field enhancements at sharp tips and corners.[7] Additionally, plasmon resonances can be conveniently tuned over a large range of the visible and near-infrared part of the electromagnetic spectrum by changing the morphology of the nanoparticle.[1,11] For these reasons, a lot of effort has been put into developing methods of synthesizing metal nanostructures with various complex shapes.[12,13]

An additional way of tuning and extending the functionalities of metal nanoparticles is the combination of different metals into one particle.[14,15] Indeed, combining the properties of two metals in bimetallic nanoparticles can lead to an improvement in plasmonic and/or catalytic properties compared to monometallic systems.[16,17] Not only the presence but also the exact distribution of the second metal defines the physical and chemical properties of the nanoparticles.[18,19] For example, for bimetallic Au−Pt core−shell nanoparticles, the optical properties and catalytic activity were shown to depend on the way Pt is distributed on the Au nanorods.[20]

Received: August 28, 2019
Accepted: October 18, 2019
Published: October 18, 2019

DOI: 10.1021/acsnano.9b06848
ACS Nano 2019, 13, 13421−13429

However, under catalytic conditions and during applications where elevated temperatures are involved, the metals can redistribute. Specifically, depending on the particular system, metals can intermix to form an alloy or instead segregate, following the process known as dealloying. These effects may alter the properties as well as the functionalities of the nanoparticles.[18,21−24] Thus, a quantitative assessment of the onset and dynamics of (de)alloying in heterogeneous metal nanoparticles is of critical importance for understanding the stability of such materials under relevant conditions. So far, studies of the elemental redistribution in nanomaterials have been primarily performed using ensemble-based techniques, such as extended X-ray absorption fine structure (EXAFS) spectroscopy,[25,26] where information is averaged between a large number of particles. On the other hand, for understanding the relationship between the stability of a nanomaterial and the microstructural properties of the particles, it is of high interest to follow the elemental redistribution on a single particle level. This poses a challenging task, as the required experimental technique should provide a high spatial resolution to obtain the information on a scale of a single nanoparticle, chemical sensitivity to retrieve the elemental distribution, and a sufficiently low acquisition time to make it feasible to follow the dynamics of the (de)alloying.

A powerful tool to study nanoscale metal redistribution *in situ* on a single particle level is transmission electron microscopy (TEM). For example, Lasserus and co-workers used high-resolution high-angle annular scanning TEM (HAADF-STEM) to study the thermally induced alloying process in spherical Au−Ag clusters.[27] By fitting an approximate density profile and making use of the atomic number contrast inherent to HAADF-STEM, the authors extracted diffusion coefficients as a function of heating temperature. Xin *et al.* monitored the atomic restructuring in spherical Pt−Co nanoparticles by high-resolution TEM.[23] Van der Hoeven and co-workers made use of TEM combined with energy-dispersive X-ray spectroscopy (EDX) to study the influence of the composition and particle size of mesoporous silica-coated Au−Ag core−shell nanorods on the alloying temperature *in situ*.[26]

Unfortunately, these techniques cannot be used for more complex geometries as they only provide 2D projections of the object, whereas for highly asymmetric hetero-nanostructures, 3D information about the metal redistribution in nanoparticles is required to fully understand how the shape, volume, and composition influence the redistribution dynamics. Electron tomography is routinely used to study nanoparticles in 3D[28,29] and can be combined with spectroscopic techniques such as EDX or electron energy-loss spectroscopy (EELS) to obtain compositional information.[30] For example, EDX tomography was implemented for complex hetero-nanostructures[31] and applied to follow the galvanic replacement reaction of Au@Ag nanoparticles.[32] Unfortunately, EDX tomography is not suited for extended *in situ* studies as such an experiment requires several hours of acquisition. Thus, to study time-resolved metal redistribution processes in bimetallic nanoparticles, a faster method is required, which will make following the dynamics of (de)alloying feasible and will reduce possible electron beam damage.

Here, we use a fast HAADF-STEM tomography approach[33] to follow the dynamics of heat-induced alloying of a Au−Ag core−shell nanorod and nanotriangles *in situ* in 3D. First, we demonstrate that quantitative analysis of HAADF-STEM tomography reconstruction allows for a reliable 3D mapping of the elemental redistribution in bimetallic particles. Next, we use the proposed method to study the influence of shape and composition on the alloying dynamics at the nanoscale by comparing a rod and a triangle shape with the same composition, as well as nanotriangles with slightly different Ag content. Furthermore, we assess the diffusion dynamics in a quantitative manner by comparing the observed experimental behavior to diffusion simulations. Our methodology enables studying the 3D metal redistribution *in situ* in complex and highly anisotropic nanostructures and is applicable to a large variety of heterogeneous nanoparticles with sufficient difference in *Z*-contrast between the two constituting elements.

RESULTS AND DISCUSSION

To investigate the heat-induced metal redistribution in anisotropic bimetallic nanoparticles with a high spatial resolution and chemical sensitivity in 3D, we performed *in situ* heating HAADF-STEM tomography of individual nanoparticles using the DENSsolutions Wildfire heating sample holder optimized for electron tomography. We studied three different Au−Ag core−shell nanoparticles of comparable volume (V) and surface-to-volume ratio (S/V): a core−shell nanorod (60 atom % Au, 40 atom % Ag, $V = 3.3 \times 10^4$ nm^3, $S/V = 0.2$ nm^{-1}), a symmetric (60 atom % Au, 40 atom % Ag, $V = 6.2 \times 10^4$ nm^3, $S/V = 0.14$ nm^{-1}), and an asymmetric (70 atom % Au, 30 atom % Ag, $V = 4.7 \times 10^4$ nm^3, $S/V = 0.15$ nm^{-1}) core−shell nanotriangle (HAADF-STEM images of the particles are displayed in Figure S1). To minimize reshaping of the nanoparticles upon heating as much as possible, the particles were coated with a 10 nm thick mesoporous silica shell.[34] The core−shell nanorod serves as an example of a shape where 2D projection methods can be sufficient for a compositional distribution analysis,[26] whereas the symmetric and asymmetric core−shell nanotriangles require a 3D investigation.

To induce alloying, the particles were heated at 450 °C *in situ* in the TEM. In order to study the alloying dynamics at intermediate steps, the alloying process was interrupted every 30 s by fast (in less than 1 s) cooling of the specimen holder to room temperature, and tomographic tilt series were acquired at each time step. After 10 time steps (resulting in 300 s of heating at 450 °C), the alloying was complete for all three studied nanoparticles. As the alloying process can be interrupted and resumed almost instantaneously by rapid cooling and heating, we expect this intermittent heating investigation to yield the same dynamics of alloying as in the case of continuous heating of the particles.

Since a conventional electron tomography experiment is quite time-consuming, we employed a fast HAADF-STEM tomography methodology, which comprises fast tilting of the specimen holder and continuous tracking of the sample.[33] In this manner, such a challenging experiment, where in total 33 tomographic series needed to be acquired, became feasible. From the obtained HAADF-STEM reconstructions we retrieved 3D compositional information on the different states of alloying for each studied nanoparticle, which we describe in the following.

It is well-known that HAADF-STEM imaging provides information about the local chemical composition of materials due to the linear dependency of the generated signal on the projected mass−thickness (for thin specimens).[35] This

DOI: 10.1021/acsnano.9b06848
ACS Nano 2019, 13, 13421−13429

property is routinely used in the analysis of elemental distribution inside heterogeneous materials and locating columns of different elements on atomic resolution images.[36−38] However, since the HAADF-STEM contrast is influenced by both composition and projected thickness of an object, application of this technique to a *quantitative* analysis of the elemental distribution has so far been limited to cases where assumptions about the geometry of the sample can be used as prior knowledge, such as flat samples, spherical, and rod-shaped particles.[27,39−41] On the other hand, arbitrary nanoparticle shapes can be studied by making use of electron tomography to eliminate the contribution of the projected thickness. As such, the resulting contrast only contains information about the elemental distribution inside a nanoparticle.

Our approach to obtain quantitative 3D compositional information at different time steps in the alloying process is illustrated in Figure 1 and proceeds as follows: we start by

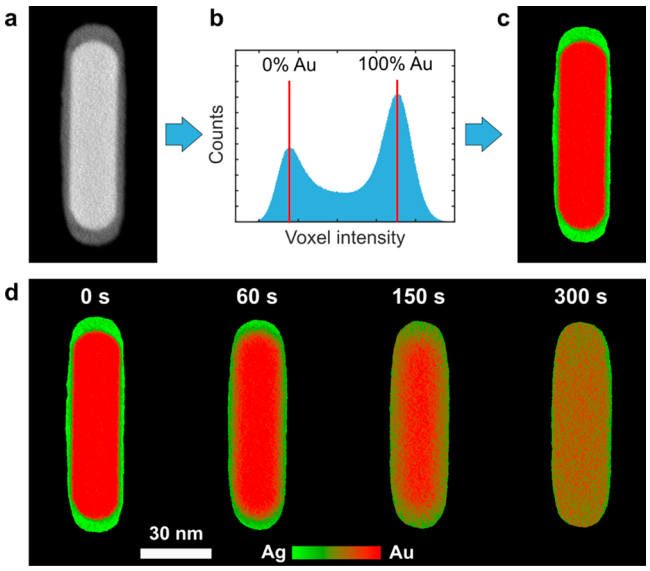

Figure 1. Schematic of the approach used to reconstruct the 3D elemental distribution inside nanoparticles upon heating. (a) Slice through the HAADF-STEM reconstruction of the Au@Ag core−shell nanorod. (b) Histogram of voxel intensities inside the particle; estimated intensity values for pure Ag and pure Au are indicated by red vertical bars. (c) Color map of the elemental distribution inside the slice of the nanorod before heating, where red corresponds to pure Au and green to pure Ag. (d) Slices through 3D compositional distributions inside the same particle at different stages of alloying upon heating at 450 °C, calculated using eq 1.

obtaining a 3D HAADF-STEM reconstruction for an object where the constituting elements are not mixed, for example, a Au−Ag core−shell nanorod. After reconstructing the 3D distribution of the HAADF-STEM signal and thus removing the contribution of the projected thickness to the contrast, the remaining intensities in the 3D reconstruction only correspond to local elemental compositions inside the object (Figure 1a). Hence, the histogram of intensities inside the particle reconstruction shows a clear bimodal distribution in the case of a two-element system (Figure 1b), where maxima correspond to the expected intensity values for each element. Since Ag has a lower atomic number than Au, voxel intensities at the lower maximum and below can be attributed to pure Ag, whereas voxel intensities at the higher maximum and above correspond to pure Au. Furthermore, the intensities lying between the maxima are related to the elemental composition of corresponding voxels by the following relation (see the Supporting Information for derivation):

$$\omega_{Au} = \frac{I - I_{Ag}}{I_{Au} - I_{Ag}} \tag{1}$$

where I is the intensity of the voxel, ω_{Au} is the relative atomic content of Au in the voxel, and I_{Au} and I_{Ag} are intensities corresponding to pure Au and Ag, respectively. Figure 1c shows a slice through the 3D elemental distribution for the initial state of the Au−Ag nanorod, obtained in this way, where red corresponds to pure Au and green to pure Ag. As can be seen, the resulting map clearly reflects the expected core−shell morphology of the particle. Equation 1 can now be used to estimate the local elemental compositions in the 3D reconstructions of the imaged object during the entire alloying process, provided that the imaging conditions were kept the same. Slices through the quantified 3D results for the nanorod after heating at 450 °C for 0, 60, 150, and 300 s are displayed in Figure 1d using the same red−green color map. The obtained elemental distribution maps display the expected gradual transition of the core−shell morphology of the nanorod into a homogeneous elemental distribution upon alloying.

To demonstrate the validity and advantages of the proposed approach, we compared the results produced by the quantification of the 3D HAADF-STEM reconstruction to EDX-based elemental mapping, a well-established technique for compositional analysis at the nanoscale (Figure 2). Details of EDX mapping can be found in the Methods section. To compare both approaches, we forward-projected the quantified 3D HAADF-STEM reconstructions along the same angle at which the 2D EDX maps were acquired. Figure 2a presents the comparison between the EDX map and the projection of the quantified HAADF-STEM reconstruction for the Au−Ag core−shell nanorod before heating. The same comparison for the nanorod after heating for 210 s is shown in Figure 2b. Both comparisons confirm a qualitative agreement between the techniques, while highlighting a significant improvement in signal-to-noise ratio for the HAADF-STEM quantification results. A quantitative comparison in Figure 2c is obtained by calculating integrated line profiles (highlighted in yellow in Figure 2a,b) through the EDX map as well as the forward projection of the quantified HAADF-STEM reconstruction at four different stages of alloying. It is evident that also an excellent quantitative agreement is observed, with noticeably less noisy line profiles for the HAADF-STEM quantification. The improved signal-to-noise ratio is not surprising, since the cross-section for the HAADF-STEM signal is generally 6 orders of magnitude higher than that of EDX.[42] The high signal-to-noise ratio of our method, combined with the fast HAADF-STEM tomography approach,[33] enabled us to retrieve a full 3D compositional distribution in a given nanoparticle in only ∼10 min. In this manner, it became possible to follow the complete timeline of the alloying process *in situ* during a single experiment for several particles. Since the experimental conditions for all particles were effectively the same, we can unambiguously relate the structure of an individual particle to the dynamics of alloying, which we will discuss in the following.

DOI: 10.1021/acsnano.9b06848
ACS Nano 2019, 13, 13421−13429

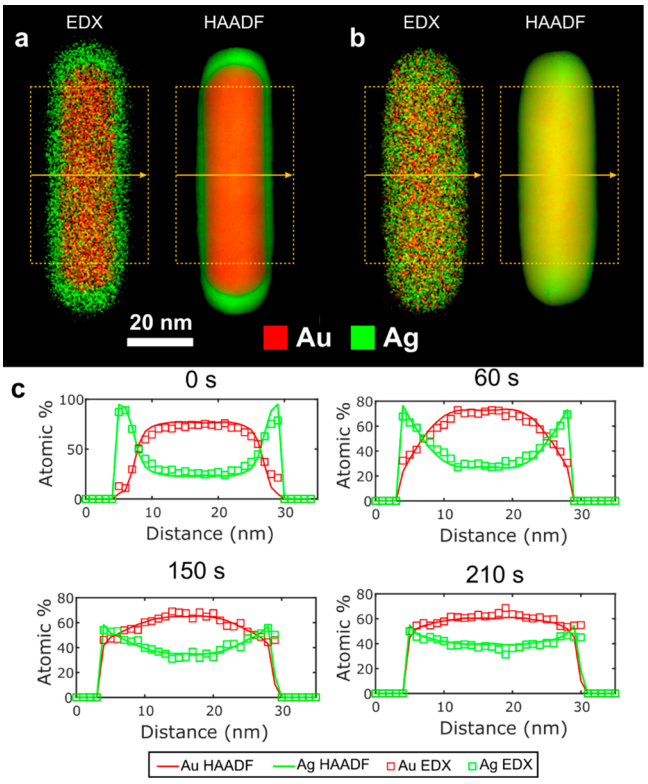

Figure 2. Comparison between 2D EDX elemental mapping and forward projection of the quantified 3D HAADF-STEM reconstruction for the same particle. (a) Initial core−shell state before heating and (b) partially alloyed particle after 210 s of heating. (c) Comparison between integrated line profiles based on the same region of the 2D EDX elemental mapping and the projection of the quantified 3D reconstruction (indicated as yellow rectangles in subfigures a and b) at different stages of alloying.

Using the methodology explained above, we obtained 11 three-dimensional compositional "snapshots" of the entire alloying process for three nanoparticles with different geometries (nanorod, symmetric, and asymmetric nanotriangles) during the same *in situ* heating experiment. Figure 3a shows the 3D visualization of the initial state of the three nanoparticles. As explained earlier, the *in situ* heating experiment was performed at 450 °C, with all nanoparticles heated for a total time of 300 s. After each heating step of 30 s, fast cooling to room temperature was used to temporarily interrupt the alloying process and to acquire a fast HAADF-STEM tomographic series. By following slices through the quantified 3D HAADF-STEM reconstructions of the nanoparticles (Figure 3b−d and Figure S3), we observed the expected progressive alloying of each particle upon heating. In the case of the nanorod and the symmetric nanotriangle, the alloying proceeds rather uniformly, whereas for the asymmetric nanotriangle the side with the thinner Ag layer appears to alloy faster.

In addition to the qualitative picture, provided by slices through the reconstructed 3D elemental distribution, the alloying dynamics can be assessed quantitatively. In this manner, practically relevant properties of particles, such as onset and rate of alloying, can be related to their size, morphology, and composition. The dynamics of particles alloying can be directly followed from the histograms showing the intensities inside the volume of a nanoparticle. In Figure 4 we show this approach using the symmetric nanotriangle as an example. As can be seen in Figure 4a, the two peaks, corresponding to the separate phases of Ag and Au for the initial core−shell particles, gradually merge together until complete homogeneity is reached (one single peak in the histogram) at the end of alloying. Thus, the spread of the distribution in the histograms can be used to quantify the alloying progress. Here, we relate the degree of alloying to the standard deviation of the distributions in the histograms. After scaling the standard deviations between 0% for the initial core−shell state and 100% for the completely homogeneous material (Figure 4b), this approach can be used to compare the dynamics of the alloying process between different particles (Figure 4c). Details of the quantification procedure can be found in the Methods section.

Figure 4c shows that our analysis method allows for monitoring small changes connected to differences in compositions and geometries. Interestingly, for the same composition, changes in morphology did not influence the alloying process drastically. The blue and yellow curves in Figure 4c compare the dynamics of alloying for the studied nanorod and symmetric nanotriangle with the same composition (60 atom % Au, 40 atom % Ag). In contrast, the alloying process is sped up for the asymmetric nanotriangle as already suggested from the 2D slices in Figure 3. The latter could possibly be related to the larger Au/Ag ratio of this particle (70 atom % Au, 30 atom % Ag) as the alloying process is composition-dependent.[26] It should be noted that the ability to capture these small differences in the alloying process demonstrates the high sensitivity of our method. The same

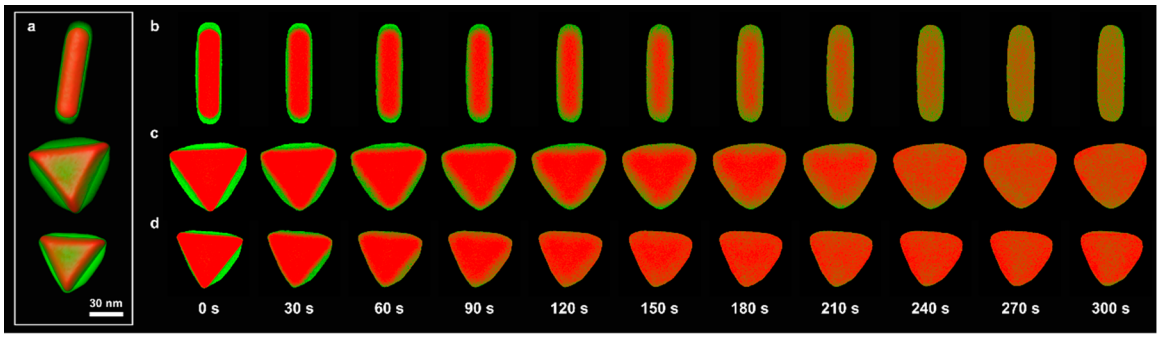

Figure 3. (a) Visualizations of 3D reconstructions for the particles studied in this work. (b−d) Slices through the 3D reconstructions of elemental distributions inside the nanorod, the symmetric, and the asymmetric nanotriangles, respectively, at different stages of alloying at 450 °C.

DOI: 10.1021/acsnano.9b06848
ACS Nano 2019, 13, 13421−13429

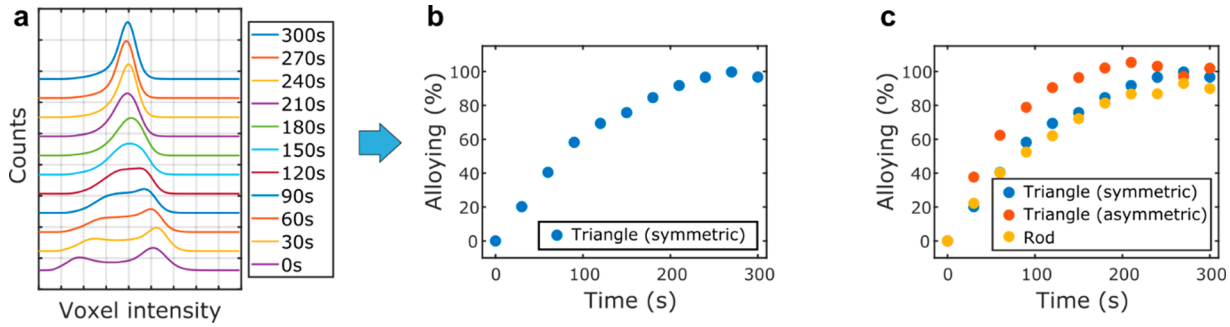

Figure 4. (a) Evolution of the histogram of voxel intensities in the reconstruction of the symmetric nanotriangle during alloying. (b) Progress of alloying for the symmetric nanotriangle during heating at 450 °C, estimated from the spread of histograms of voxel intensities in the reconstruction. (c) Comparison of the alloying dynamics for the nanorod, the symmetric, and the asymmetric nanotriangles.

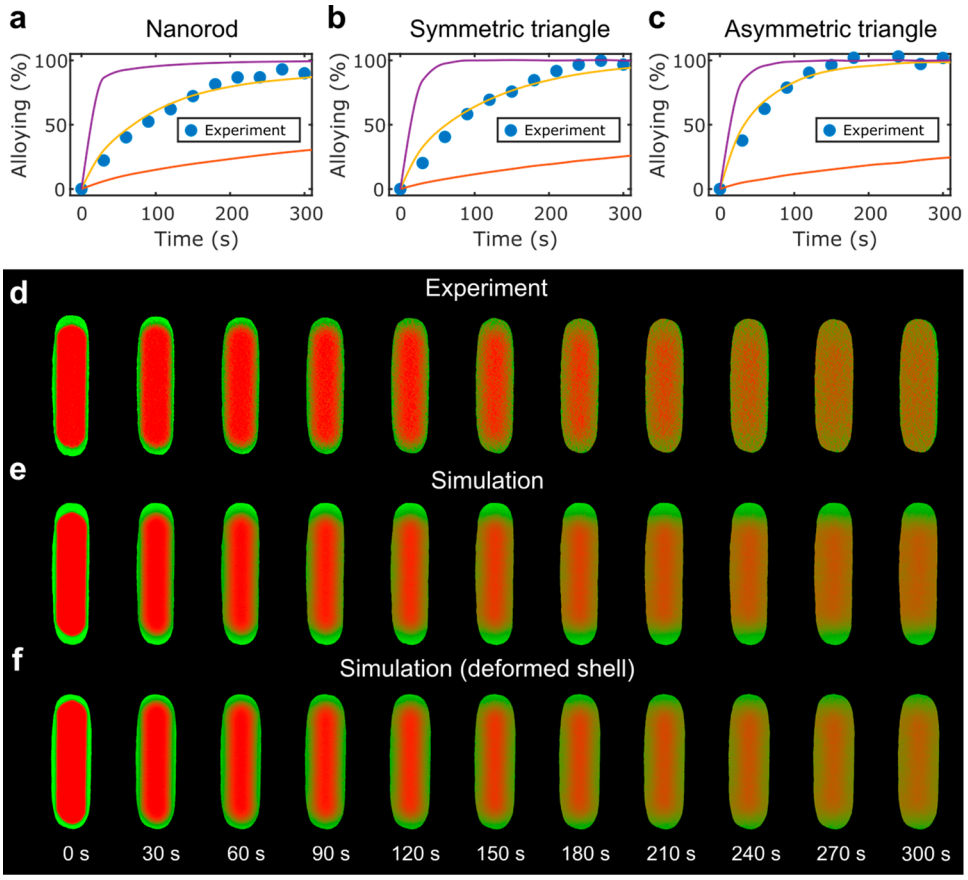

Figure 5. Comparison of diffusion simulations and experiments. (a−c) Progress of alloying quantified from the experimental data (blue points) and simulation results for the nanorod, symmetric, and asymmetric nanotriangles, respectively, using three different diffusion coefficients (solid lines). Yellow curves correspond to diffusion coefficients of (a) 1×10^{-19} m^2/s, (b) 1.5×10^{-19} m^2/s, and (c) 3×10^{-19} m^2/s, which produced the best match with the experimental data. For all particles, purple curves correspond to a diffusion coefficient of 1.0×10^{-18} m^2/s and orange curves to 1.0×10^{-20} m^2/s. (d) Slices through the experimentally determined 3D elemental distribution in the nanorod at different stages of alloying. (e) Slices through the simulated 3D elemental distribution using the optimal diffusion coefficient. (f) Slices through the 3D diffusion simulations for which a deformed Ag shell was used.

cannot be achieved by 2D EDX mapping, for which the low signal-to-noise ratio hampers the comparison between the three particles (Figure S5). Additionally, 2D projection methods are inherently insufficient for asymmetric particle shapes, since elemental distribution along the projection direction cannot be retrieved.

To gain more insight into the alloying process and diffusion dynamics in the studied nanoparticles, we compared our experimental results to 3D diffusion simulations. As a starting configuration we used the quantified HAADF-STEM reconstruction of the initial state of each nanoparticle. The elemental redistribution over the course of 300 s was then simulated using a discretization of Fick's law over the experimental voxel grid while imposing no-flow boundary conditions on the surface of the particles (see the Methods section for details). Next, the alloying dynamics was quantified for the simulation results in the same manner as for the experimental data. To make simulations directly comparable to the experiments, it

DOI: 10.1021/acsnano.9b06848
ACS Nano 2019, 13, 13421−13429

was necessary to incorporate the artifacts related to the tomography experiment in the simulation prior to quantification (see the Methods section for discussion). Diffusion coefficients of 1×10^{-19}, 1.5×10^{-19}, and 3×10^{-19} m^2/s produced a good match of the quantified alloying process obtained from simulations to the experimental result for the nanorod, symmetric, and asymmetric nanotriangles, respectively (yellow curves in Figure 5a−c). For a comparison, a smaller value of 1×10^{-20} m^2/s (orange curves) or a larger value of 1×10^{-18} m^2/s (purple curves) results in a clear mismatch between simulations and experiments. The diffusion coefficients estimated in this way fit well to tabulated bulk values. Indeed, for diffusion of Au in Ag, which is the limiting process in our experiment since Ag in Au diffusion is faster, tabulated bulk diffusion coefficients are around 2×10^{-19} m^2/s at 450 °C.[43,44] Interestingly, although the size-dependent increase in the alloying speed is a concern for the stability of Au−Ag core−shell nanoparticles with diameters below 5 nm,[45] the alloying dynamics of particles studied in this work (with characteristic sizes larger than 20 nm) follow the bulk material behavior. Although studying the size-dependent, shape-dependent, and composition-dependent alloying dynamics in more detail lies beyond the scope of this work, our methodology allows for doing so on a single nanoparticle basis and will be valuable for future work in that direction.

In Figure 5d,e, we compare slices through the experimentally obtained 3D reconstruction of the elemental distribution in the nanorod to the elemental redistribution simulation, corresponding to the yellow curve in Figure 5a. Although generally a good agreement is observed, the diffusion at the tips of the rod happens faster than predicted by simulations. Especially at later stages, alloying on the particle scale goes faster than predicted by Fickian diffusion, which can also be seen for the other particle shapes (Figure S6). This discrepancy can be most likely attributed to slight reshaping of the nanoparticles upon heating, as the mesoporous silica shell cannot prevent the deformation of the surface completely.[46] Indeed, by comparing the 3D shapes of the nanorod before and after the experiment we observed a volume redistribution from the tips to the central part of the nanorod (Figure S7), which is also visible in the experimental orthoslices. Since Ag is more mobile than Au and has a lower melting point (962 °C against 1064 °C for Au), the main reshaping occurs in the Ag shell before alloying sets in, creating a more uniform Ag layer around the Au core. To illustrate the effect of such reshaping on alloying, we made diffusion simulations after setting the initial shape of the Ag shell to the final deformed shape of the particle. From the results depicted in Figure 5f, it is visible that in the case of the deformed shell alloying proceeds more uniformly in all parts of the particle, similar to what is observed in the experiment. This observation illustrates that alloying at the nanoscale is a complex process, and factors such as surface diffusion need to be taken into account in theoretical models of this process.

CONCLUSIONS

In summary, we showed that a quantitative analysis of HAADF-STEM tomography allows for a reliable determination of the 3D elemental distribution in bimetallic nanoparticles. The combination of this method with a fast tomographic acquisition enabled us to obtain a full 3D compositional distribution for a nanoparticle in only 10 min. In this manner, it became feasible to follow the 3D alloying dynamics of individual nanoparticles with different shapes and compositions upon heating with a time step of 30 s at 450 °C. For a given composition, the shape of the nanoparticle did not influence the alloying process significantly, whereas the change in relative composition altered the alloying speed. By comparing our results to Fickian diffusion simulations, we obtained a quantitative description of the alloying dynamics through estimating the diffusion coefficients on a single particle level. Additionally, comparison to the simulation indicated that the alloying process in the nanoparticles is more complex than predicted by simple Fickian diffusion, and additional factors, such as surface diffusion, have to be taken into account for its accurate theoretical modeling.

METHODS

Nanoparticles Synthesis. Mesoporous silica-coated Au-core Ag-shell nanorods were synthesized following the procedure reported previously.[26] Shortly, Au nanorods, obtained by seed-mediated $HAuCl_4$ reduction, were coated by a mesoporous silica shell and oxidatively etched using H_2O_2, and the void formed between the Au core and silica shell was filled with Ag using $AgNO_3$ reduction. For the Au-core Ag-shell nanotriangles synthesis, the triangular Au seeds were obtained according to the Scrabelli *et al.*[47] The resulting nanoparticles were coated by a Ag shell using $AgNO_3$ reduction and covered by a thin layer of mesoporous silica. The detailed description of all synthetic procedures can be found in the Supporting Information.

Heating, Tomographic Series Acquisition, and Reconstruction. All experiments were performed using a ThermoFisher Tecnai Osiris electron microscope operated at 200 kV in HAADF-STEM mode using a DENSsolutions tomography heating holder with MEMS-based heating chips. We used Wildfire Nanochip design with a high temperature precision and homogeneity.[48] Tilt series for the nanoparticles were acquired between −75° and 75° using a fast tomography approach, described elsewhere.[33] The projection images were acquired with 50 pA beam current and 1 s exposure time. Image resolution constituted 1024 × 1024 pixels with a pixel size of 0.212 nm. The obtained series were aligned using cross-correlation, and 3D reconstructions were obtained using 20 iterations of the Expectation Maximization (EM) algorithm, as implemented in Astra Toolbox.[49]

Determination of 3D Elemental Distribution. Elemental distributions in the particles were calculated from the 3D HAADF-STEM reconstructions (see Figure S2 for the schematic). First, intensities I_{Ag} and I_{Au}, corresponding to pure Ag and Au, were estimated from the two respective maxima on histograms of 3D reconstructions for the initial core−shell state of the particles. In the next step, voxels corresponding to a vacuum around the particles were masked on each reconstruction. The vacuum mask was obtained by using the $\frac{I_{Ag}}{2}$ value as an intensity threshold and applying a 3D morphological closing with a radius of 5 pixels to smooth the boundaries of the mask. This particular threshold value was chosen to produce the maximum separation between the maxima for vacuum (0 intensity) and silver (I_{Ag} intensity) voxels. Finally, the elemental compositions of each voxel in a particle were calculated by applying eq 1, while intensities higher than I_{Au} and lower than I_{Ag} were set to 100% and 0% of Au, respectively.

EDX-Based Elemental Mapping. EDX-based elemental maps were recorded using the Super-X detector in the ThermoFisher Tecnai Osiris electron microscope operated at 200 kV over the course of 10 min with an electron beam current of 140 pA. The integrated line profiles obtained from the EDX maps were quantified using the ζ-factor method, which was shown to yield higher accuracy than the more conventional k-factor-based quantification.[50] ζ-factors were measured before the experiment following the procedure of Zanaga *et al.*[50]

Calculation of Alloying Degree from 3D Data. To calculate the degree of alloying for the nanoparticles at particular time steps we used the fact that the spread of voxel intensity values on the

DOI: 10.1021/acsnano.9b06848
ACS Nano 2019, 13, 13421−13429

histograms of 3D HAADF-STEM reconstructions of the particles decreases during their gradual homogenization upon alloying (see Figure S4). Precisely, the following procedure was used: (1) Voxels corresponding to vacuum were masked in the reconstructions to remove their contribution to the spread of intensities. (2) The spread of the intensities for each resulting histogram was calculated as the standard deviation of all intensity values. (3) The standard deviations at each time step for a particle were normalized between the values corresponding to the initial core−shell (0%) and a perfectly homogeneous (100%) state of the particle:

$$a_i = \frac{\sigma_i - \sigma_0}{\sigma_\infty - \sigma_0} \times 100\% \tag{2}$$

where a_i and σ_i are, respectively, the degree of alloying and the standard deviation of voxel intensities at time step i, and σ_0 and σ_∞ are estimated standard deviations of voxel intensities in the initial core−shell and perfectly homogeneous states of the particle. To obtain the value of σ_∞, the spread of intensities in the 3D reconstruction of a perfectly alloyed particle has to be simulated. To achieve this, we first set all intensities inside the 3D reconstruction of the particle at the last time step to the average of all intensity values (which corresponds to the intensity of a perfectly alloyed material). Next, to take into account the additional spread, coming from the limited number of projection images available for the tomographic reconstruction, we obtained projections of the simulated perfectly alloyed particle for the same set of angles as used in the experiments. Next, a 3D reconstruction based on these images was calculated. Another source of intensity spread in the experimental reconstructions is the result of blurring of sharp edges due to the imperfect alignment of images in the tilt series. To incorporate this effect, we applied a Gaussian blurring to the simulated reconstruction until the spread of the sharp edges matched the experimental reconstructions. Simulating other sources of experimental error, such as Poisson noise, resulted in only negligible changes in the spread of the intensity values.

Diffusion Simulations. Simulations of 3D elemental redistribution were based on discrete approximation of Fick's second law and were implemented using Forward-Time Central-Space (FTCS) finite difference method. Precisely, the elemental distribution was defined on a uniform cubical grid, which resulted directly from applying the proposed quantification method to the 3D reconstructions of the particles. Fick's second law was approximated using the following convolution operation:

$$\frac{dC}{dt} = D\cdot(\Delta * C) \tag{3}$$

where $C = C(x, y, z, t)$ is the 3D elemental distribution, D is the diffusion coefficient, and $*$ is a spatial convolution operation. Δ is the discrete Laplace operator, defined as a 3D array Δ_{ijk}:

$$\Delta_{ij1} = \begin{bmatrix} 0 & 0 & 0 \\ 0 & 1 & 0 \\ 0 & 0 & 0 \end{bmatrix}, \quad \Delta_{ij2} = \begin{bmatrix} 0 & 1 & 0 \\ 1 & -6 & 1 \\ 0 & 1 & 0 \end{bmatrix}, \quad \Delta_{ij3} = \begin{bmatrix} 0 & 0 & 0 \\ 0 & 1 & 0 \\ 0 & 0 & 0 \end{bmatrix} \tag{4}$$

Starting from the initial state, the elemental distribution was iteratively updated based on eq 3 using the Euler's method:

$$C(t + \Delta t) = C(t) + \frac{dC}{dt}(t)\cdot\Delta t \tag{5}$$

The size of the time step Δt was set to be small enough to ensure the convergence of the method. At all time steps a no-flow condition was imposed on the boundary of the particle by locally setting the appropriate coefficients of the Δ operator to zero. The boundary was estimated in the same manner as the vacuum mask described in the elemental quantification procedure. All the described calculations were implemented in the Matlab programming environment.

The starting elemental distribution for the simulations was obtained from the reconstructions of the particles at the initial time steps. The shape of the Au core was obtained by using $\frac{I_{Ag} + I_{Au}}{2}$ intensity as a threshold, whereas for the outer shape of the particle, the $\frac{I_{Ag}}{2}$ threshold was used. Edges of both masks were smoothed by applying a 3D morphological closing with a radius of 5 pixels. Content of gold was set to 100% inside the core, and to 0% between the core and the outer shell of the particles.

When obtaining the alloying curves based on the results of diffusion simulations, the effects of limited projection angles and blurring were incorporated at each time step of the simulation, in the same way as was explained for the simulations of the perfectly alloyed states of the particles. Next, the spread of voxel intensities was calculated and normalized between the values for the core−shell and the perfectly alloyed state of the particles using the same procedure as for the experimental data.

ASSOCIATED CONTENT

Supporting Information

The Supporting Information is available free of charge on the ACS Publications website at DOI: 10.1021/acsnano.9b06848.

Detailed description of nanoparticles synthesis, derivation of eq 1, slices through the calculated 3D elemental distribution for experimental data and simulations of all particles and time steps, comparison to 2D EDX alloying investigation, and a visualization of particles reshaping upon alloying (PDF)

AUTHOR INFORMATION

Corresponding Author

*E-mail: Sara.Bals@uantwerpen.be.

ORCID

Xiaobin Xie: 0000-0003-0190-1807

Sara Bals: 0000-0002-4249-8017

Author Contributions

[‖]A.S. and W.A. contributed equally.

Notes

The authors declare no competing financial interest.

ACKNOWLEDGMENTS

This project has received funding from the European Commission (grant 731019, EUSMI) and European Research Council (ERC Consolidator Grants 815128, REALNANO; 770887, PICOMETRICS; 648991, 3MC; and ERC Advanced Grant 291667, HierarSACol). This project has also received funding from the European Union's Horizon 2020 research and innovation program under grant agreement 823717, ESTEEM3. W.A. acknowledges an Individual Fellowship funded by the Marie Sklodowska-Curie Actions (MSCA) in Horizon 2020 program (grant 797153, SOPMEN). E.B. acknowledges a postdoctoral grant 12T2719N from the Research Foundation Flanders (FWO, Belgium). X.X. acknowledges financial support from the EU H2020-MSCA-ITN-2015 project 676045, MULTIMAT. The authors also acknowledge financial support by the Research Foundation Flanders (FWO grants G038116N, G026718N, and G036915N).

REFERENCES

(1) Pelton, M.; Aizpurua, J.; Bryant, G. Metal-Nanoparticle Plasmonics. *Laser Photonics Rev.* **2008**, *2*, 136−159.

(2) Linic, S.; Christopher, P.; Ingram, D. B. Plasmonic-Metal Nanostructures for Efficient Conversion of Solar to Chemical Energy. *Nat. Mater.* **2011**, *10*, 911−921.

(3) Louis, C.; Pluchery, O. *Gold Nanoparticles for Physics, Chemistry, and Biology*; Imperial College Press: London, 2012.

DOI: 10.1021/acsnano.9b06848
ACS Nano 2019, 13, 13421−13429

(4) Baffou, G.; Quidant, R. Thermo-Plasmonics: Using Metallic Nanostructures as Nano-Sources of Heat. *Laser Photonics Rev.* **2013**, *7*, 171−187.
(5) Dreaden, E. C.; Alkilany, A. M.; Huang, X.; Murphy, C. J.; El-Sayed, M. A. The Golden Age: Gold Nanoparticles for Biomedicine. *Chem. Soc. Rev.* **2012**, *41*, 2740−2779.
(6) Desantis, C. J.; Skrabalak, S. E. Size-Controlled Synthesis of Au/Pd Octopods with High Refractive Index Sensitivity. *Langmuir* **2012**, *28*, 9055−9062.
(7) Reguera, J.; Langer, J.; Jiménez de Aberasturi, D.; Liz-Marzán, L. M. Anisotropic Metal Nanoparticles for Surface Enhanced Raman Scattering. *Chem. Soc. Rev.* **2017**, *46*, 3866−3885.
(8) Zijlstra, P.; Chon, J. W. M.; Gu, M. Five-Dimensional Optical Recording Mediated by Surface Plasmons in Gold Nanorods. *Nature* **2009**, *459*, 410−413.
(9) Atwater, H. A.; Polman, A. Plasmonics for Improved Photovoltaic Devices. *Nat. Mater.* **2010**, *9*, 205−213.
(10) Linic, S.; Aslam, U.; Boerigter, C.; Morabito, M. Photochemical Transformations on Plasmonic Metal Nanoparticles. *Nat. Mater.* **2015**, *14*, 567−576.
(11) Kelly, K. L.; Coronado, E.; Zhao, L. L.; Schatz, G. C. The Optical Properties of Metal Nanoparticles: The Influence of Size, Shape, and Dielectric Environment. *J. Phys. Chem. B* **2003**, *107*, 668−677.
(12) Rycenga, M.; Cobley, C. M.; Zeng, J.; Li, W.; Moran, C. H.; Zhang, Q.; Qin, D.; Xia, Y. Controlling the Synthesis and Assembly of Silver Nanostructures for Plasmonic Applications. *Chem. Rev.* **2011**, *111*, 3669−3712.
(13) Li, N.; Zhao, P.; Astruc, D. Anisotropic Gold Nanoparticles: Synthesis, Properties, Applications, and Toxicity. *Angew. Chem., Int. Ed.* **2014**, *53*, 1756−1789.
(14) Hou, S.; Hu, X.; Wen, T.; Liu, W.; Wu, X. Core-Shell Noble Metal Nanostructures Templated by Gold Nanorods. *Adv. Mater.* **2013**, *25*, 3857−3862.
(15) Albrecht, W.; van der Hoeven, J. E. S.; Deng, T.-S.; de Jongh, P. E.; van Blaaderen, A. Fully Alloyed Metal Nanorods with Highly Tunable Properties. *Nanoscale* **2017**, *9*, 2845−2851.
(16) Edwards, J.; Solsona, B.; Landon, P.; Carley, A.; Herzing, A.; Kiely, C.; Hutchings, G. Direct Synthesis of Hydrogen Peroxide from H_2 and O_2 Using TiO_2-Supported Au-Pd Catalysts. *J. Catal.* **2005**, *236*, 69−79.
(17) DeSantis, C. J.; Weiner, R. G.; Radmilovic, A.; Bower, M. M.; Skrabalak, S. E. Seeding Bimetallic Nanostructures as a New Class of Plasmonic Colloids. *J. Phys. Chem. Lett.* **2013**, *4*, 3072−3082.
(18) Liao, H.; Fisher, A.; Xu, Z. J. Surface Segregation in Bimetallic Nanoparticles: A Critical Issue in Electrocatalyst Engineering. *Small* **2015**, *11*, 3221−3246.
(19) Zugic, B.; Wang, L.; Heine, C.; Zakharov, D. N.; Lechner, B. A. J.; Stach, E. A.; Biener, J.; Salmeron, M.; Madix, R. J.; Friend, C. M. Dynamic Restructuring Drives Catalytic Activity on Nanoporous Gold-Silver Alloy Catalysts. *Nat. Mater.* **2017**, *16*, 558−564.
(20) Zheng, Z.; Tachikawa, T.; Majima, T. Single-Particle Study of Pt-Modified Au Nanorods for Plasmon- Enhanced Hydrogen Generation in Visible to Near-Infrared Region. *J. Am. Chem. Soc.* **2014**, *136*, 6870−6873.
(21) Tao, F.; Grass, M. E.; Zhang, Y.; Butcher, D. R.; Renzas, J. R.; Liu, Z.; Chung, J. Y.; Mun, B. S.; Salmeron, M.; Somorjai, G. A. Reaction-Driven Restructuring of Rh-Pd and Pt-Pd Core-Shell Nanoparticles. *Science* **2008**, *322*, 932−934.
(22) Tao, F.; Salmeron, M. *In Situ* Studies of Chemistry and Structure of Materials in Reactive Environments. *Science* **2011**, *331*, 171−174.
(23) Xin, H. L.; Alayoglu, S.; Tao, R.; Genc, A.; Wang, C.-M.; Kovarik, L.; Stach, E. A.; Wang, L.-W.; Salmeron, M.; Somorjai, G. A.; Zheng, H. Revealing the Atomic Restructuring of Pt-Co Nanoparticles. *Nano Lett.* **2014**, *14*, 3203−3207.
(24) Pramanik, S.; Chattopadhyay, S.; Das, J. K.; Manju, U.; De, G. Extremely Fast Au-Ag Alloy-Dealloy Associated Reversible Plasmonic Modifications in SiO_2 Films. *J. Mater. Chem. C* **2016**, *4*, 3571−3580.
(25) Frenkel, A. I. Applications of Extended X-Ray Absorption Fine-Structure Spectroscopy to Studies of Bimetallic Nanoparticle Catalysts. *Chem. Soc. Rev.* **2012**, *41*, 8163−8178.
(26) van der Hoeven, J. E. S.; Welling, T. A. J.; Silva, T. A. G.; van den Reijen, J. E.; La Fontaine, C.; Carrier, X.; Louis, C.; Van Blaaderen, A.; de Jongh, P. E. *In Situ* Observation of Atomic Redistribution in Alloying Gold−Silver Nanorods. *ACS Nano* **2018**, *12*, 8467−8476.
(27) Lasserus, M.; Schnedlitz, M.; Knez, D.; Messner, R.; Schiffmann, A.; Lackner, F.; Hauser, A. W.; Hofer, F.; Ernst, W. E. Thermally Induced Alloying Processes in a Bimetallic System at the Nanoscale: AgAu Sub-5 nm Core-Shell Particles Studied at Atomic Resolution. *Nanoscale* **2018**, *10*, 2017−2024.
(28) Goris, B.; Bals, S.; Van den Broek, W.; Carbó-Argibay, E.; Gómez-Graña, S.; Liz-Marzán, L. M.; Van Tendeloo, G. Atomic-Scale Determination of Surface Facets in Gold Nanorods. *Nat. Mater.* **2012**, *11*, 930−935.
(29) Van Tendeloo, G.; Bals, S.; Van Aert, S.; Verbeeck, J.; Van Dyck, D. Advanced Electron Microscopy for Advanced Materials. *Adv. Mater.* **2012**, *24*, 5655−5675.
(30) Goris, B.; Polavarapu, L.; Bals, S.; Van Tendeloo, G.; Liz-Marzán, L. M. Monitoring Galvanic Replacement through Three-Dimensional Morphological and Chemical Mapping. *Nano Lett.* **2014**, *14*, 3220−3226.
(31) Zanaga, D.; Altantzis, T.; Polavarapu, L.; Liz-Marzán, L. M.; Freitag, B.; Bals, S. A New Method for Quantitative XEDS Tomography of Complex Heteronanostructures. *Part. Part. Syst. Charact.* **2016**, *33*, 396−403.
(32) Polavarapu, L.; Zanaga, D.; Altantzis, T.; Rodal-Cedeira, S.; Pastoriza-Santos, I.; Pérez-Juste, J.; Bals, S.; Liz-Marzán, L. M. Galvanic Replacement Coupled to Seeded Growth as a Route for Shape-Controlled Synthesis of Plasmonic Nanorattles Galvanic Replacement Coupled to Seeded Growth as a Route for Shape-Controlled Synthesis of Plasmonic Nanorattles. *J. Am. Chem. Soc.* **2016**, *138*, 11453−11456.
(33) Vanrompay, H.; Bladt, E.; Albrecht, W.; Béché, A.; Zakhozheva, M.; Sánchez-Iglesias, A.; Liz-Marzán, L. M.; Bals, S. 3D Characterization of Heat-Induced Morphological Changes of Au Nanostars by Fast *In Situ* Electron Tomography. *Nanoscale* **2018**, *10*, 22792−22801.
(34) Albrecht, W.; Deng, T. S.; Goris, B.; van Huis, M. A.; Bals, S.; van Blaaderen, A. Single Particle Deformation and Analysis of Silica-Coated Gold Nanorods before and after Femtosecond Laser Pulse Excitation. *Nano Lett.* **2016**, *16*, 1818−1825.
(35) Williams, D. B.; Carter, C. B. *Transmission Electron Microscopy*; Springer: New York, 2009.
(36) van den Bos, K. H. W.; Altantzis, T.; De Backer, A.; Van Aert, S.; Bals, S. Recent Breakthroughs in Scanning Transmission Electron Microscopy of Small Species. *Adv. Phys. X* **2018**, *3*, 1480420.
(37) Gauquelin, N.; van den Bos, K. H. W.; Béché, A.; Krause, F. F.; Lobato, I.; Lazar, S.; Rosenauer, A.; Van Aert, S.; Verbeeck, J. Determining Oxygen Relaxations at an Interface: A Comparative Study between Transmission Electron Microscopy Techniques. *Ultramicroscopy* **2017**, *181*, 178−190.
(38) Schryvers, D.; Salje, E. K. H.; Nishida, M.; De Backer, A.; Idrissi, H.; Van Aert, S. Quantification by Aberration Corrected (S)TEM of Boundaries Formed by Symmetry Breaking Phase Transformations. *Ultramicroscopy* **2017**, *176*, 194−199.
(39) Liu, W.; Sun, K.; Wang, R. *In Situ* Atom-Resolved Tracing of Element Diffusion in NiAu Nanospindles. *Nanoscale* **2013**, *5*, 5067−5072.
(40) Chi, M.; Wang, C.; Li, D.; Stamenkovic, V. R.; Lei, Y.; Lupini, A.; More, K. L.; Allard, L. F.; Wang, G.; Markovic, N. M. Surface Faceting and Elemental Diffusion Behaviour at Atomic Scale for Alloy Nanoparticles during *In Situ* Annealing. *Nat. Commun.* **2015**, *6*, 1−9.
(41) Van Den Bos, K. H. W.; De Backer, A.; Martinez, G. T.; Winckelmans, N.; Bals, S.; Nellist, P. D.; Van Aert, S. Unscrambling Mixed Elements Using High Angle Annular Dark Field Scanning

DOI: 10.1021/acsnano.9b06848
ACS Nano 2019, 13, 13421−13429

Transmission Electron Microscopy. *Phys. Rev. Lett.* **2016**, *116*, 246101.
(42) MacArthur, K. E.; Slater, T. J. A.; Haigh, S. J.; Ozkaya, D.; Nellist, P. D.; Lozano-Perez, S. Quantitative Energy-Dispersive X-Ray Analysis of Catalyst Nanoparticles Using a Partial Cross Section Approach. *Microsc. Microanal.* **2016**, *22*, 71−81.
(43) Mallard, W. C.; Gardner, A. B.; Bass, R. F.; Slifkin, L. M. Self-Diffusion in Silver-Gold Solid Solutions. *Phys. Rev.* **1963**, *129*, 617−625.
(44) Noah, M. A.; Flötotto, D.; Wang, Z.; Reiner, M.; Hugenschmidt, C.; Mittemeijer, E. J. Interdiffusion in Epitaxial, Single-Crystalline Au/Ag Thin Films Studied by Auger Electron Spectroscopy Sputter-Depth Profiling and Positron Annihilation. *Acta Mater.* **2016**, *107*, 133−143.
(45) Shibata, T.; Bunker, B. A.; Zhang, Z.; Meisel, D.; Vardeman, C. F.; Gezelter, J. D. Size-Dependent Spontaneous Alloying of Au-Ag Nanoparticles. *J. Am. Chem. Soc.* **2002**, *124*, 11989−11996.
(46) Buffat, P.; Borrel, J.-P. Size Effect on the Melting Temperature of Gold Partlcles. *Phys. Rev. A: At., Mol., Opt. Phys.* **1976**, *13*, 2287−2298.
(47) Scarabelli, L.; Coronado-Puchau, M.; Giner-Casares, J. J.; Langer, J.; Liz-Marzán, L. M. Monodisperse Gold Nanotriangles: Size Control, Large-Scale Self-Assembly, and Performance in Surface-Enhanced Raman Scattering. *ACS Nano* **2014**, *8*, 5833−5842.
(48) DENSsolutions Wildfire In Situ Heating Systems for TEM Platforms: Product Brochure. https://denssolutions.com/products/wildfire/brochure/ (accessed Aug 28, 2019).
(49) van Aarle, W.; Palenstijn, W. J.; De Beenhouwer, J.; Altantzis, T.; Bals, S.; Batenburg, K. J.; Sijbers, J. The ASTRA Toolbox: A Platform for Advanced Algorithm Development in Electron Tomography. *Ultramicroscopy* **2015**, *157*, 35−47.
(50) Zanaga, D.; Altantzis, T.; Sanctorum, J.; Freitag, B.; Bals, S. An Alternative Approach for ζ-Factor Measurement Using Pure Element Nanoparticles. *Ultramicroscopy* **2016**, *164*, 11−16.

DOI: 10.1021/acsnano.9b06848
ACS Nano 2019, 13, 13421−13429